JOURNAL OF AIRCRAFT
Vol. 47, No. 5, September–October 2010

# Parametric Study for Hovering Performance of a Coaxial Rotor Unmanned Aerial Vehicle

Jaewon Lee,* Sanghyun Chae,† Sejong Oh,‡ and Kwanjung Yee§
*Pusan National University, Busan 609-735, Republic of Korea*

DOI: 10.2514/1.46460

**This paper proposes a reliable aerodynamics analysis method designed for a coaxial rotor unmanned aerial vehicle. It is then used to investigate the effects of the selected design parameters on the hovering performance of the coaxial rotor. A coaxial rotor performance analysis code based on the source-doublet panel method is developed, and its accuracy is verified to be sufficient by comparing its results to various test data. Through a parametric study for the rotor design parameters, such as radius, twist, and taper, the effect of each parameter on the coaxial rotor design is investigated and a statistical analysis for the resulting data is conducted. The results show that the diameter has the biggest impact on the hovering performance of a coaxial rotor, whereas the taper has the biggest impact if the diameter is fixed. Based on these findings, a revised rotor platform is proposed, with 33% improvement of the figure of merit over the baseline concept, which implies that the optimal design significantly improves the performance of the rotor under development.**

## Nomenclature

| | | |
|---|---|---|
| $A_{ij}, B_{ij}, C_{ij}$ | = | influence coefficients |
| AI | = | autorotation index |
| $C_d$ | = | section drag coefficient |
| $C_{d_{\min}}$ | = | section minimum drag coefficient |
| $C_{d_0}$ | = | section zero-lift drag coefficient |
| $C_l$ | = | section lift coefficient |
| $C_P$ | = | power coefficient |
| $C_{\mathrm{PM}}$ | = | pitching moment coefficient |
| $C_p$ | = | pressure coefficient |
| $C_{p_0}$ | = | incompressible pressure coefficient |
| $C_{\mathrm{RM}}$ | = | rolling moment coefficient |
| $C_T$ | = | thrust coefficient |
| $C_{\mathrm{YM}}$ | = | yawing moment coefficient |
| full | = | full-scale rotor |
| DL | = | disk loading |
| $h$ | = | perpendicular distance from vortex element to evaluation point, m |
| $M$ | = | Mach number |
| $\hat{n}$ | = | normal vector |
| $\mathbf{P}$ | = | position vector of any point |
| $p$ | = | pressure, $\mathrm{N/m^2}$ |
| $R$ | = | radius of blade, m |
| $Re$ | = | Reynolds number |
| $\mathbf{r}$ | = | distance vector from a point $\mathbf{P}$, m |
| $r_c$ | = | vortex's core radius, m |
| $r_{c0}$ | = | initial core size of the vortex segment, m |
| $S$ | = | boundaries |
| sub | = | subscale rotor |
| $t$ | = | time, s |
| $\mathbf{V}_f$ | = | momentary local velocity of the $(X, Y, Z)$ system's origin |
| $\mathbf{V}_0$ | = | velocity vector of the $(x, y, z)$ system's origin |
| $v_{\mathrm{ref}}$ | = | magnitude of the kinematic velocity |
| $\mathbf{v}_{\mathrm{rel}}$ | = | relative velocity vector within the $(x, y, z)$ system |
| $W$ | = | weight |
| $X, Y, Z$ | = | global reference frame coordinates |
| $x, y, z$ | = | body-fixed reference frame coordinates |
| $\alpha$ | = | Lamb–Oseen coefficient, 1.25643 |
| $\Gamma$ | = | circulation |
| $\delta$ | = | average effective viscosity coefficient |
| $\zeta$ | = | wake age, rad |
| $\theta$ | = | collective pitch angle, deg |
| $\theta_{\mathrm{tw}}$ | = | twist angle, deg |
| $\kappa$ | = | induced-power factor |
| $\mu$ | = | rotor advance ratio |
| $\mu_\Phi$ | = | doublet |
| $\nu$ | = | kinematic viscosity |
| $\rho$ | = | fluid density |
| $\sigma$ | = | rotor solidity, $N_b c/\pi R$ |
| $\sigma_\Phi$ | = | source |
| $\Phi$ | = | velocity potential |
| $\psi$ | = | azimuth angle |
| $\Omega$ | = | rate of rotation of the body's frame of reference, rad/s |
| $\infty$ | = | infinity, far field |

## I. Introduction

WITH the threats by terrorism, crime issues and budget pressures increasing, the military needs to attain new technological capabilities to more effectively perform their missions. A small and agile Unmanned Aerial Vehicle (UAV) that can be used for overhead surveillance, remote sensing and communications relay is a concept that is attracting much attention. In response to the increasing needs for the compact multipurpose UAV, Pusan National University has begun the development of a UAV prototype and its operating system. The primary mission of the UAV is to conduct surveillance over a small area for more than half an hour. The size of the platform for the UAV is required to be small enough to be carried by one person. The small size also implies low weight, which is required for easy handling in the field. This platform would provide three-dimensional mobility to a variety of interchangeable mission packages. After the conceptual tradeoff studies on various configurations, the coaxial rotor system turns out to be a viable alternative. The coaxial rotor configuration has the advantages of its compact dimension and the potential for greater lifting efficiency in addition to hovering and loitering capabilities of a conventional helicopter, which are particularly important for battlefield surveillance and urban intelligence gathering.

Received 23 July 2009; revision received 8 June 2010; accepted for publication 15 June 2010. 

*Researcher, Research Institute of Mechanical Technology, San 30 Jangjeon 2(i)-dong Geumjong-gu.
†Graduate Student, Department of Aerospace Engineering.
‡Professor, Department of Aerospace Engineering. Member AIAA.
§Associate Professor, Department of Aerospace Engineering; daedalus@pusan.ac.kr. Member AIAA.

The studies on the coaxial rotor configuration have been carried out for many years. Leishman [1] mentioned that Sikorsky proposed a coaxial rotor system applicable to a variety of helicopters. Preator et al. [2] suggested the use of a coaxial rotor on the monotiltrotor in 2004. The monotiltrotor concept has a single counter-rotating coaxial rotor system, which is tilted forward during the cruise. Although the coaxial rotor configurations have been widely used in various European countries, the aerodynamic characteristics of coaxial rotor configuration has not been fully understood yet. As shown in Coleman's [3] comprehensive review on the experimental and analytical studies of the coaxial rotors, the research conducted in the 1990s heavily relied on the experiments, whereas few theoretical studies were performed. Moreover, it has been long debated over whether or not the coaxial rotor configuration is more efficient than the other configurations. The detailed aerodynamic characteristics of the coaxial rotor, such as wake structures and inter-rotor interactions, are not fully understood yet.

However, the recent advancement in computational methodologies enables us to model complex aerodynamics with substantial confidence. Recently, the numerical methods [3–6] ranging from panel methods to computational fluid dynamics (CFD) methods have been applied to the coaxial rotor studies, and the results demonstrated reasonable agreement with the experimental data. Theoretically, CFD is an ultimate method, because the Navier–Stokes equations can model every aspect of the aerodynamic flowfields with fewer physical assumptions. The performance of a coaxial rotor under the conditions of hovering, steady forward flight, level and coordinated turns was numerically investigated by Kim and Brown [4] using the vorticity transport method (VTM), which is based on a time-dependent computational solution to the vorticity-velocity form of the Navier–Stokes equations. With the use of the convection algorithm and adaptive-grid system, the VTM method is more efficient than the existing CFD methods, however, it is still computationally burdensome compared to the panel methods.

The Panel methods are considered to be more efficient and less diffusive numerical schemes and still widely used for helicopter aerodynamic analysis. Several studies to analyze the performance of the multirotor system using the panel methods have been accomplished. Leishman and Ananthan [5] developed the blade element momentum theory (BEMT) for coaxial rotor and solved the local air loads over the upper and lower rotors. A vortex-lattice method (VLM) coupled with a free-vortex wake analysis was employed to validate the results obtained from the BEMT and a validation conclusion indicated that the results exhibited good agreements with the experimental data. Wachspress and Quackenbush [6] also attempted to enhance the CHARM (Comprehensive Hierarchical Aeromechanics Rotorcraft Model, the comprehensive rotorcraft analysis code that uses a constant vorticity contour free-wake model) to facilitate the aerodynamic and aeroacoustic design of the coaxial rotor systems. Simulation results indicated that there exist substantial differences in the performance and wake behavior between the single and coaxial rotor systems. Although some previous studies have been proven to be successful and computationally efficient, all of these singularity methods use a vortex-lattice representation of the blade and are not capable of predicting the effect of the thickness of the rotor blade. Moreover, the complex configurations with varying sectional airfoil have been rarely considered. Accordingly, the present study employs the source-doublet panel method, which is able to consider complex blade configurations.

The primary aim of the present work is to investigate the aerodynamic performance of the coaxial rotor system in detail with respect to various design parameters. An optimal coaxial rotor configuration is sought based on the understanding of the use of the latest analytical methods. To this end, a reliable analysis tool for coaxial rotor configuration was first developed and thoroughly validated against the available experimental data. Several design parameters such as twist, taper and ratio of rotor radii were chosen to investigate the effects on the aerodynamic performance under the hovering condition. The differential collective pitch angle can be a viable candidate parameter for improving performance of coaxial rotor. However, it is not selected as the design parameter. It is because the combination of collective angles of upper and lower rotors is fixed for a given thrust as long as the calculated results are obtained under the condition of zero net yawing moment. Based on the parametric studies, a modified rotor configuration is suggested and its aerodynamic performance is compared with that of the baseline rotor configuration. The hovering performance is primarily investigated in this study, because the condition of $\mu < 0.1$ must be satisfied for the required mission: the reconnaissance and loiter for 10 min at the altitude of 30 m, as summarized in Fig. 1. This implies the aerodynamic performance is very similar to that under the hovering condition.

## II. Numerical Analysis Approach

When the aerodynamic performance of a UAV with complex blade configurations and varying sectional airfoil is analyzed using the panel method, there are issues that need to be considered. First, with the use of a vortex-lattice description of the blade, the existing VLM, the widely used method for rotor aerodynamic analysis, is unable to account for the effect of the thickness of the rotor blade. Second, in the analysis of a rotor in hovering mode, instability in the wake often occurs, as shown in Fig. 2a, due to the interaction between the strong starting vortex created at the early calculation because of the impulsive starting and the wake created at the rotor hub. This is a general problem that occurs in the hovering rotor analysis using the free-wake based panel method. Figure 2b reveals that this problem disappears when the rotor climbs even at a small rate. Furthermore, without accounting for viscosity, the panel methods usually correct the profile drag by using the lookup table. The two-dimensional airfoil aerodynamic table used in this case is usually obtained by conducting experiments or computing at the Reynolds number regime where actual helicopters operate. Consequently, the difference of the Reynolds number regimes between a UAV rotor and a two-dimensional airfoil represented by an aerodynamic table can make a significant error in the profile power prediction. In the following section, the numerical techniques will be described to resolve those problems.

### A. Source-Doublet Panel Method with Time-Marching Free-Wake Model

To account for the effects of the blade thickness and complicated blade shapes, the source-doublet panel method, which is often used for analyzing the whole body of a fixed wing aircraft, is adopted in this work. The general solution of the Laplace equation is given as a sum of the source and doublet distribution over the body's surface and its wakes:

$$\Phi(\mathbf{P}) = \frac{-1}{4\pi}\int_{\text{body}}\left[\sigma_\Phi\left(\frac{1}{r}\right) - \mu_\Phi \hat{n}\cdot\nabla\left(\frac{1}{r}\right)\right]\mathrm{d}s + \frac{1}{4\pi}\int_{\text{wake}}\left[\mu_\Phi \hat{n}\cdot\nabla\left(\frac{1}{r}\right)\right]\mathrm{d}s + \Phi_\infty(\mathbf{P}) \tag{1}$$

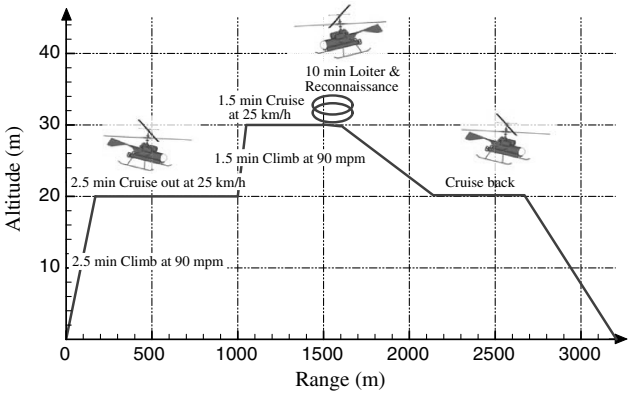


**Fig. 1 Generic mission profile for the coaxial rotor UAV.**

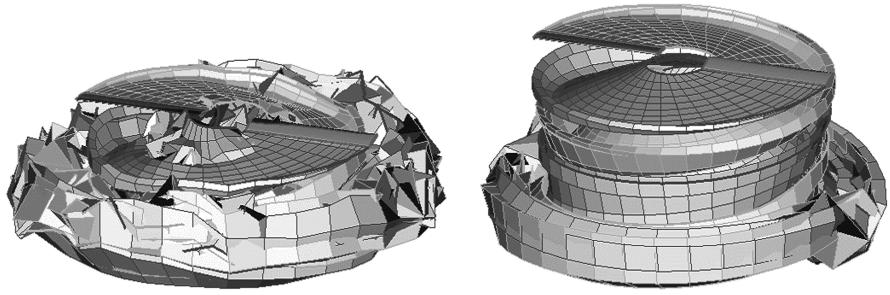

a) Hovering rotor wake b) Climbing rotor wake: $V_{climb}=0.03M_{tip}$

**Fig. 2 Hovering rotor wake instability.**

To determine a unique solution, the source distribution is set to be equal to the local kinematic velocity. The source strength can be given by Eq. (2):

$$\sigma_\Phi = -\hat{n}\cdot(\mathbf{V}_0 + \mathbf{v}_{\text{rel}} + \boldsymbol{\Omega}\times\mathbf{r}) \tag{2}$$

To establish the boundary value problem, the local velocity at each point on the body has to satisfy the zero flow condition across the body surface, as shown in Eq. (3):

$$\nabla\Phi\cdot\hat{n} - \mathbf{V}_f\cdot\hat{n} = 0 \tag{3}$$

From the Kutta condition, the latest wake doublets can be expressed in terms of the unknown surface doublets, given by Eq. (4):

$$\mu_{\Phi,\text{wake}} = \mu_{\Phi,\text{upper}} - \mu_{\Phi,\text{lower}} \tag{4}$$

When specified at the body's $N$ collocation points, Eq. (3) will reduce to

$$[A_{ij}](\mu_k) = (\text{RHS}_k) = [B_{ij}](\sigma_k) + [C_{ij}](\mu_{wk}) \tag{5}$$

This matrix has a nonzero diagonal and has a stable numerical solution. The resulting pressures can be computed by using the Bernoulli equation, which yields

$$C_p = -\frac{(\nabla\Phi)^2}{v_{\text{ref}}^2} + \frac{2}{v_{\text{ref}}^2}[\mathbf{V}_0 + \boldsymbol{\Omega}\times\mathbf{r}]\cdot\nabla\Phi - \frac{2}{v_{\text{ref}}^2}\frac{\partial\Phi}{\partial t} \tag{6}$$

Additionally, in order to correct the compressibility effect over the calculated pressure coefficient, the Karman–Tsien theorem is applied, as shown in Eq. (7). Although the Prandtl–Glauert theorem is the simplest one, it has a tendency of underestimating the pressure coefficient as compared to test data, whereas the Karman–Tsien theorem accounts for the nonlinear aspects of the flow and is able to predict the pressure coefficients more accurately [7]:

$$C_p = \frac{C_{p_0}}{\sqrt{1-M^2} + \left(\frac{M^2}{1+\sqrt{1-M^2}}\right)\frac{C_{p_0}}{2}} \tag{7}$$

A wake model is needed to simulate the deformation of the wake caused by the contraction. The free-wake concept allows the vorticity to evolve in a free motion, and represents the unsteady aerodynamics using a physics-based approach. The free-wake model includes the wake-relaxation scheme and time-marching scheme. The wake-relaxation scheme includes specifying the wake geometry at the beginning of the solution process, and solving the problem for the fixed wake. It computes the induced velocity at each wake control point. The location of the wake moves with the induced velocity and an artificial time step. The time-marching method is modified from the wake-relaxation scheme with an assumption of a physical time step. The wake is shed from the trailing edge, and its size increases linearly proportional to the time step [8]. This method is more efficient for the numerical computation, due to the fact that only the induced velocity of the actual wake points has to be computed. Given the number of time step, the time-marching method is about twice as fast as the wake-relaxation scheme [8]; therefore, the time-marching free-wake model is selected to be applied in this work.

The wake doublet panel with constant strength is replaced by the equivalent vortex ring, because it is known to be more efficient in calculating the induced velocity with the use of the Biot–Savart law. This approach is based on the method presented by Hess [9], in which the constant-strength doublet element is equivalent to a constant-strength vortex ring placed at the panel edges. The total induced velocity at a point is obtained through summating the velocity induced by each vortex segment. The induced velocity is given by the Biot–Savart law. The singularity problem in the vortex center is resolved by the vortex core model. Leishman et al. [10] concluded that the Vatistas et al. [11] vortex model with $n = 2$ best fits the experimental data. In the present methods, the Vatistas et al. [11] vortex model is used to prevent vortex center singularity. With the Vatistas et al. [11] vortex model, the equation for the induced velocity is reduced to

$$\mathbf{V} = \frac{\Gamma}{4\pi}\frac{h}{(r_c^{2n} + h^{2n})^{1/n}}(\cos\theta_1 - \cos\theta_2)\hat{e} \tag{8}$$

where $n$ is an integer (Fig. 3).

The total 288 (24 chordwise by 12 spanwise) source-doublet panels are used on each blade, and at the end of the computation, the number of wake panels reaches up to 8600 (12 spanwise by 36 azimuthal by 20 revolution). The computation time required for 20 rotor revolutions is approximately 35 h on a PC with Intel Core 2 Quad Q9400.

### B. Wake Instability

The stability of the rotor wake is an important characteristic of the hovering performance analyzed using a free-wake model. There have been various attempts to deal with such a stability problem. Lee [12] used the slow-starting approach with the downward induced velocity on the wake up to 2 revolutions. Rosen and Graber [13] assumed that the vortex filament at the hub travels at the speed of 75% of the vortex filament's speed at the tip. Summa and Maskew [14] calculated the free wake at the advanced ratio of 0.05 and then corrected the calculation for hovering conditions with the use of the test data. Bagai and Leishman [15] stated that the artificial large vortex core radius needs to avoid the abrupt change of the angle of attack, due to

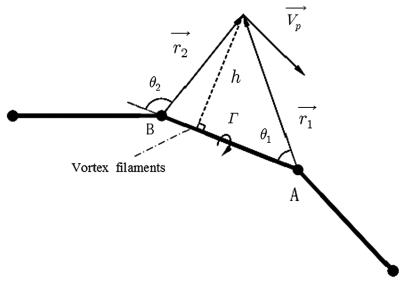


**Fig. 3 Schematic illustration of the velocity induced by a straight-line vortex element.**

the large induced velocity created between the adjacent vortices and tip vortex very close to the blade. Furthermore, Quaranta et al. [16] rapidly increased the core radius of the starting vortex and inner vortex in order to achieve a stable and accurate solution. However, those methods applied to VLM without accounting for thickness are ineffective for source-doublet panel method that accounts for thickness. Besides the research activities using the methods discussed before, for example, the climb speed is assigned as 5% of the tip speed and followed by the hovering condition with a small vortex core intentionally set. The results showed that these attempts did not improve the efficiency. In this study, a more stable solution has been obtained by applying the slow-starting approach suggested in [12] for the first two revolutions, which facilitates the reduction of initial vortex instability commonly found in time-marching free-wake method. The vortex core diffusion effects are modeled using the following empirical equation:

$$r_c(\zeta) = \sqrt{r_{c0}^2 + 4\alpha\delta\nu\zeta/\Omega} \tag{9}$$

where $r_{c0}$ is the initial core size, $\alpha$ is the Lamb–Oseen coefficient (1.25643), $\delta$ is the average effective viscosity coefficient, and $\nu$ is the kinematic viscosity.

Figure 4 depicts the calculated tip wake geometry of a two-bladed single rotor for the cases with and without the vortex core diffusion model that Caradonna and Tung [17] used in their experiments. In the case without the vortex core diffusion model, it can be seen that the instability of the tip wake appears after one revolution. In addition, the wake asymmetry appearing on (both of) the two rotor blade sides is observed after some revolutions. On the other hand, in the case using the vortex core diffusion model, the stable tip wake geometry is formed, as shown in Fig. 4b. In addition, it is observed that the rotor wake trajectory is significantly stabilized when the vortex core model is included. The wake descent and contraction rates are compared against the available experimental data of Caradonna and Tung in Fig. 5. As can be found in the figure, the wake contraction rate is in good agreement with the experiments. However, the wake descent rate in the present calculation is found to be slightly steeper than the experiment.

### C. Reynolds Number Scaling for Drag Estimation

Since a source-double panel code is not able to account for the viscous drag, a two-dimensional table describing the aerodynamic characteristics of the airfoil should be provided in order to correctly calculate the profile rotor power. The table is usually given at a high Reynolds number regime ($10^6$–$10^7$). It is necessary to scale the given airfoil table to match the current Reynolds number, because the drag (which can be eventually converted to the profile rotor power) is sensitive to Reynolds number. Wachspress and Quackenbush [6] stated that it is sufficient to use Eq. (10) as long as the practical range of Reynolds number, except at very low Reynolds numbers below 300,000 to 500,000:

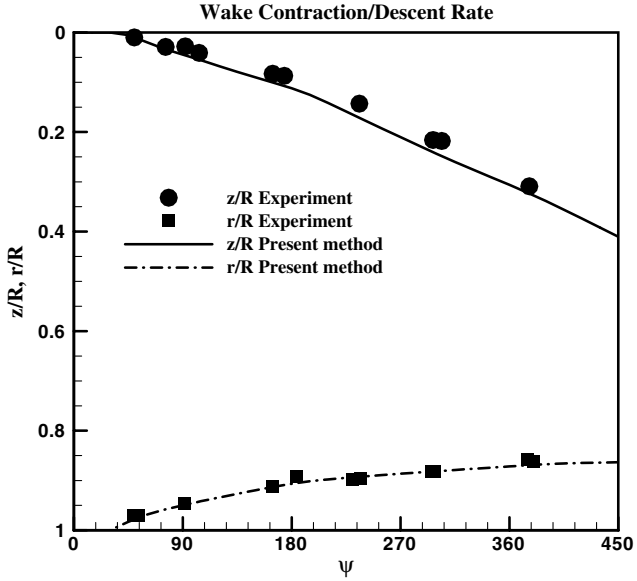


**Fig. 5 Wake contraction/descent rate ($M_{\text{tip}} = 0.439$, $\theta_c = 8\,\text{deg}$).**

$$C_{d_{\min,\text{sub}}} = C_{d_{\min,\text{full}}} + C_{d_{\min,\text{full}}}(Re_{\text{full}}/Re_{\text{sub}})^{1/5} \tag{10}$$

The cases studied with and without the Reynolds number scaling on the test data will be compared in part of the next section, in which Harrington's [18] rotor will be discussed.

## III. Code Validations

The numerical code employed in the paper was validated against the measured rotor performance. The experimental data were collected from Harrington [18]. Harrington's coaxial rotor is composed of two counter-rotating two-blade rotors with $H/D = 0.19R$. The rotor system 1 has the solidity ($\sigma$) of 0.027 with two blades for each rotor ($2\sigma = 0.054$ in coaxial rotor), and the rotor system 2 has a solidity of 0.076 ($2\sigma = 0.152$ in coaxial rotor). Both sets of rotors are untwisted, but rotor 1 has tapered blades with varying thickness along the span. The information associated with the platform and thickness ratio of the blade is shown in Fig. 6. The airfoil used in Harrington's experiments belongs to the NACA four-digit series; however, it is not sufficient to get the drag information only by looking up the corresponding 2-D airfoil data table, since the thickness of the rotor blade varies with the radial positions. The aerodynamic drag of the nonstandard airfoil sections can be obtained from the empirical correlation explained by Leishman [1].

Figure 7 shows the aerodynamic performance of two coaxial rotors in hovering. The difference in the thrust and power, with respect to the drag correction due to Reynolds number, is shown in

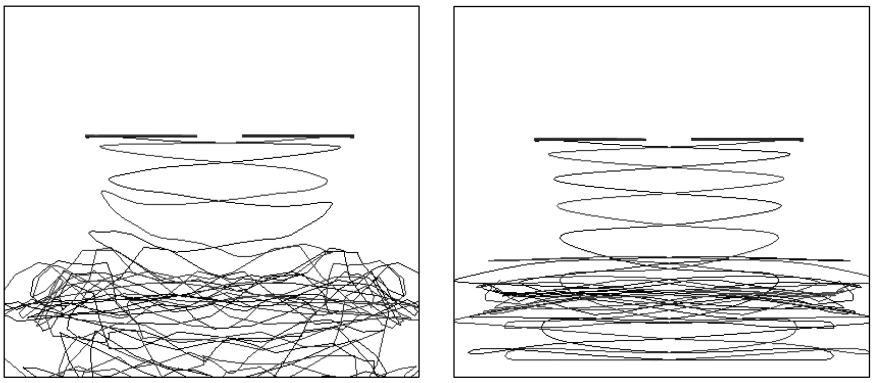

**a) Without the vortex core diffusion model** **b) With the vortex core diffusion model**

**Fig. 4 Effect of the vortex core diffusion; tip wake geometry of a two-blade single rotor.**

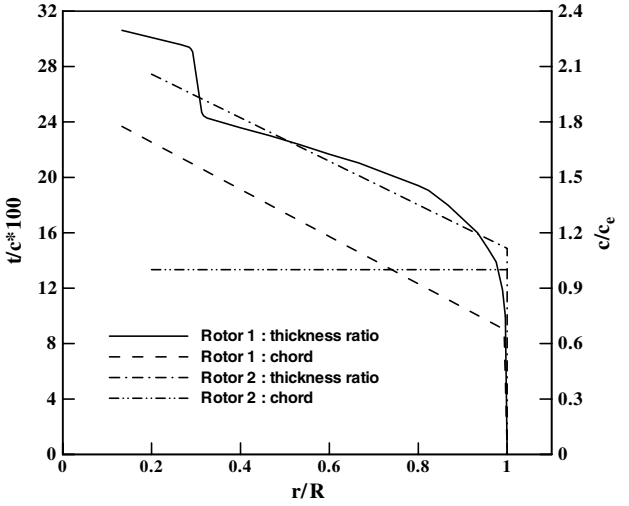


**Fig. 6 Variation of rotor blade chord and thickness ratio of Harrington's [18] rotors.**

this figure. The Reynolds numbers depend on the rotor tip speed for Harrington [18] rotors 1 and 2 are $8 \times 10^5$ and $2.3 \times 10^6$, respectively. The reference Reynolds number of the aerodynamic data given in the C81 format is $5.2 \times 10^6$, and the drag coefficients are corrected based on the local Reynolds number using Eq. (10). It can be seen that the drag correction based on Reynolds number has a substantial impact on the overall aerodynamic performance. This is because the Reynolds number of a small UAV is usually order-of-magnitude smaller than that of a full-scale vehicle.

The calculated contraction and axial descent rate of the tip vortices generated by a coaxial rotor in hovering are compared against the experimental data shown in [19]. The coaxial rotor used in the experiment consists of two articulated rotors with rectangular planform and NACA0012 airfoil section. The tip vortex trajectory obtained from the method used in this study is shown in Fig. 8 and is the time-averaged location over one revolution. Figure 8 shows the test results for the rotors with the vertical space $H/D$ of 0.105. In the experiment, the collective pitch angles of the upper and lower rotors are fixed at 9 and 10°, respectively, for which a torque balance can be achieved.

With the use of Kim and Brown's [4] strategy in this study, the results are obtained by trimming each rotor to match the thrust in the experiment, rather than merely having the rotors using the same collective pitch as in the experiment. As can be seen in Fig. 8, the overall agreement between the calculated and experimental data is good, although the number of the experimental data points is not enough for the rigorous comparison. The error bars in the figure indicate the range of variation of the location over one revolution. The results exhibit the physical trend observed by the previous researchers. This trend indicates that the axial descent rate of the tip

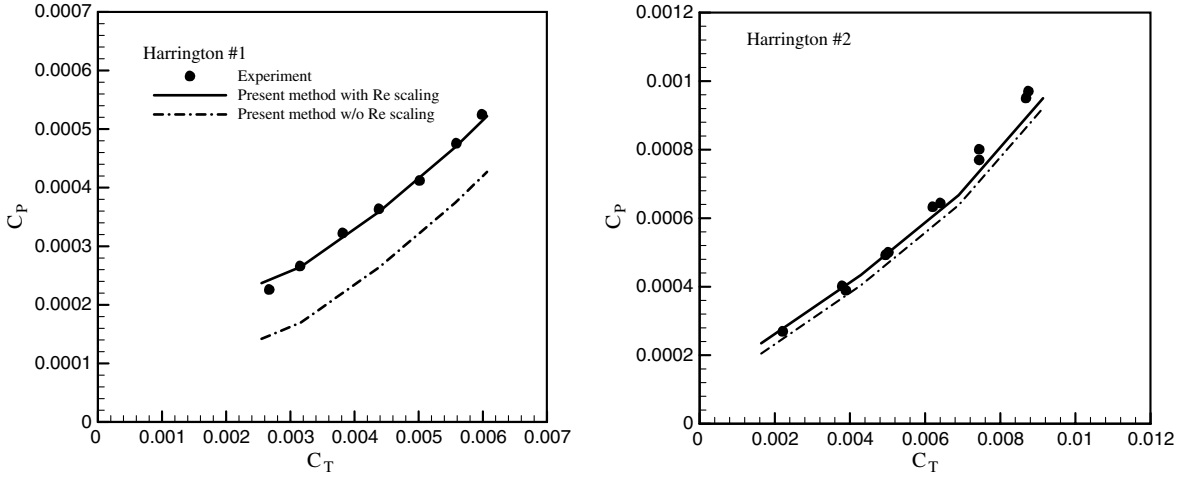


**a) $C_T$ vs. $C_P$ with Harrington's rotor 1** **b) $C_T$ vs. $C_P$ with Harrington's rotor 2**

**Fig. 7 Comparison between present method and Harrington's [18] experiments.**

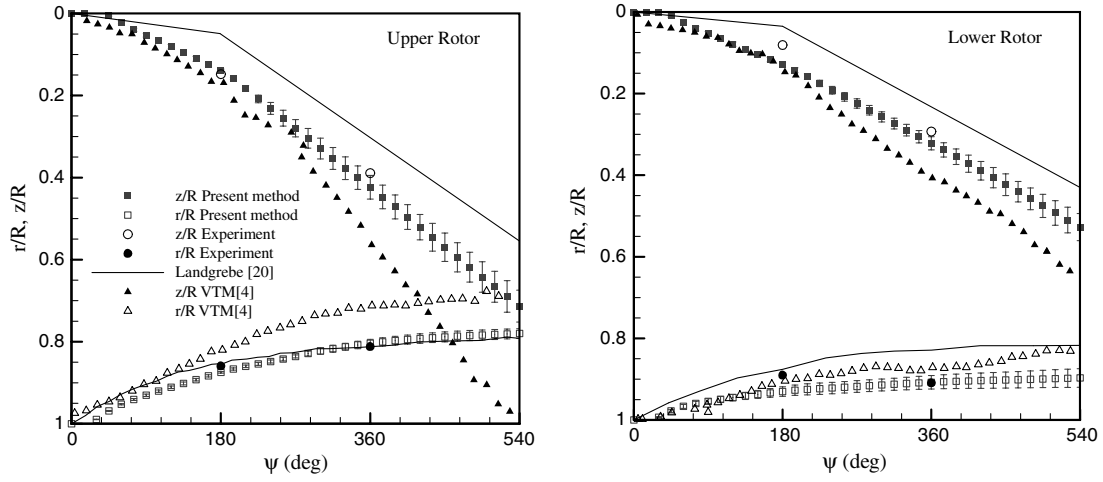


**a) Tip wake trajectory of upper rotor** **b) Tip wake trajectory of lower rotor**

**Fig. 8 Correlation of tip vortex trajectory of a coaxial rotor against Nagashima and Nakanishi's [19] experimental data.**

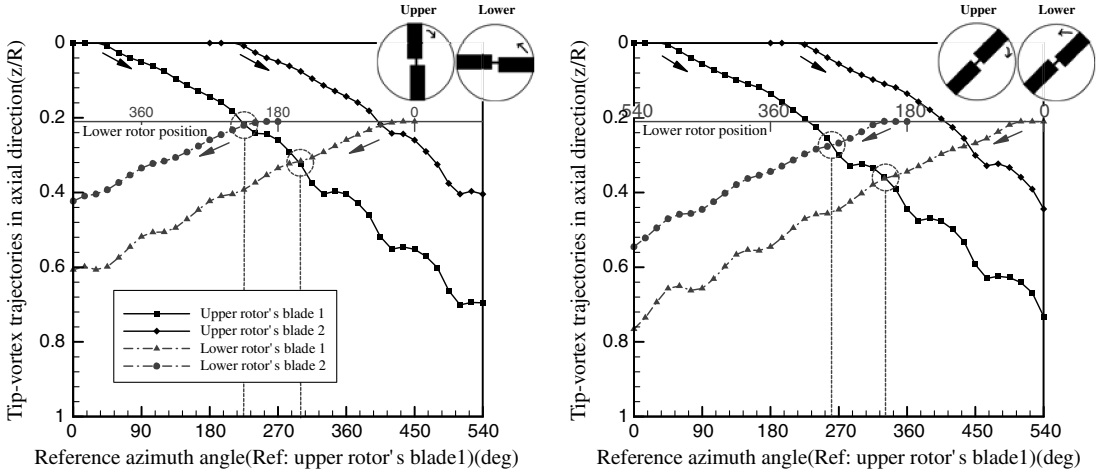


**a) 90 deg phase difference** **b) No phase difference**

**Fig. 9 Tip vortex trajectory of coaxial rotor in axial direction.**

vortices for both rotors is faster than that of a single rotor with the same thrust obtained by Landgrebe's [20] prescribed wake model (solid lines). However, the computational results show that the radial contraction of the tip vortices associated with the lower rotor proceeds more slowly than that of a single rotor. Since the upper and lower rotors in a coaxial rotor are rotating in opposite directions, the relative position between the rotors varies depending on the azimuth angle. Figure 9 depicts the tip vortex trajectories at two representative azimuth angles. It can be seen that the tip vortex trajectories of both rotors are oscillating. This is due to the varying relative position of the upper and lower rotor blades. From Fig. 9a, one can see that when there is a 90 deg phase difference between the upper and the lower rotor blades, the tip vortex generated by the upper rotor blade 1 passes the lower rotor plane at around 225 deg and meets another tip vortex generated by the lower rotor. On the other hand, Fig. 9b shows that they intersect at 260 deg if the rotors are in the same phase. The relative movement of both rotors causes the up-and-down oscillation of the vortices. Because of the lack of sufficient test data, the actual occurrence of such tip vortex trajectories, which are not clearly mentioned in Brown's work, are difficult to verify; hence, further research is needed.

The calculated coaxial rotor performances for the forward flight are compared against the wind-tunnel data obtained from Dingeldein's [21] investigation. The rotor used in this study is identical to Harrington's [18] rotor 1. The experimental trim strategy that the differential collective pitch uses to trim the rotor to zero net yawing moment is replicated in the study. To represent the effects of the parasite drag from the fuselage in the trim state of the experimental system, the forward tilt of the rotor was adjusted to produce a sufficient forward force to overcome the drag created by a fuselage with the equivalent flat-plate area of 10 $ft^2$. The trim calculation is automated by using a Newton–Raphson iterative method, as shown in Eq. (11):

$$\begin{Bmatrix} \Delta\theta_{0_1} \\ \Delta\theta_{0_2} \\ \Delta\theta_{1c} \\ \Delta\theta_{1s} \end{Bmatrix} = \begin{bmatrix} \frac{\partial C_T}{\partial\theta_{0_1}} & \frac{\partial C_T}{\partial\theta_{0_2}} & \frac{\partial C_T}{\partial\theta_{1c}} & \frac{\partial C_T}{\partial\theta_{1s}} \\ \frac{\partial C_{\mathrm{PM}}}{\partial\theta_{0_1}} & \frac{\partial C_{\mathrm{PM}}}{\partial\theta_{0_2}} & \frac{\partial C_{\mathrm{PM}}}{\partial\theta_{1c}} & \frac{\partial C_{\mathrm{PM}}}{\partial\theta_{1s}} \\ \frac{\partial C_{\mathrm{RM}}}{\partial\theta_{0_1}} & \frac{\partial C_{\mathrm{RM}}}{\partial\theta_{0_2}} & \frac{\partial C_{\mathrm{RM}}}{\partial\theta_{1c}} & \frac{\partial C_{\mathrm{RM}}}{\partial\theta_{1s}} \\ \frac{\partial C_{\mathrm{YM}}}{\partial\theta_{0_1}} & \frac{\partial C_{\mathrm{YM}}}{\partial\theta_{0_2}} & \frac{\partial C_{\mathrm{YM}}}{\partial\theta_{1c}} & \frac{\partial C_{\mathrm{YM}}}{\partial\theta_{1s}} \end{bmatrix}^{-1} \times \begin{Bmatrix} C_T^{\mathrm{desired}} - C_T \\ -C_{\mathrm{PM}} \\ -C_{\mathrm{RM}} \\ -C_{\mathrm{YM}} \end{Bmatrix} \tag{11}$$

where $C_T$, $C_{\mathrm{PM}}$, $C_{\mathrm{RM}}$, and $C_{\mathrm{YM}}$ are thrust coefficient, pitching moment coefficient, rolling moment coefficient, and yawing moment coefficient, respectively. Control inputs $\theta_{0_1}$ and $\theta_{0_2}$ are the collective pitch angles of upper and lower rotor, and $\theta_{1c}$ and $\theta_{1s}$ denote lateral cyclic angle and longitudinal pitch angle, respectively. As indicated in the equation, unlike the collective pitch angle, cyclic control inputs $\theta_{1c}$ and $\theta_{1s}$ are set to be the same on both rotors. Target value of moment coefficients are 0, and thrust is $C_T^{\mathrm{desired}}$. Newton–Raphson method iteratively searches the increments of control inputs using gradient information of control inputs to performances, until it reaches the target performances, which means that the second terms of RHS become 0.

In Fig. 10, the control inputs required to trim the rotor are listed. The trim values of the VTM simulation [4] are used as the initial values, and the trim converges after $3 \sim 4$ iterations. The initial values may have an influence on the convergence rate, and the values that are significantly different from the trim solution often cause the trim to fail.

Figure 11 shows a comparison of the power consumption against the advance ratio at a uniform thrust coefficient of 0.0048 for the present simulation, VTM simulation [4] and Dingeldein's [21] measurements, implying that the experimental power trends for the coaxial rotor are well replicated by using the present method. It is also shown that the tendency of the present calculations exhibits a very good agreement with the experimental data, and the present estimations are more accurate than the VTM results, which show an overall underestimation of the power coefficient at all the advance ratios. Kim and Brown [4] argued that this inaccurate power consumption is due to the uncertainties existing in the profile drag characteristics of the rotor. Although both, VTM and present method, use the same lookup table to estimate the profile power, the method used in this study appears to reproduce the test data with better agreement, due to its better estimation of the wake trajectory, as

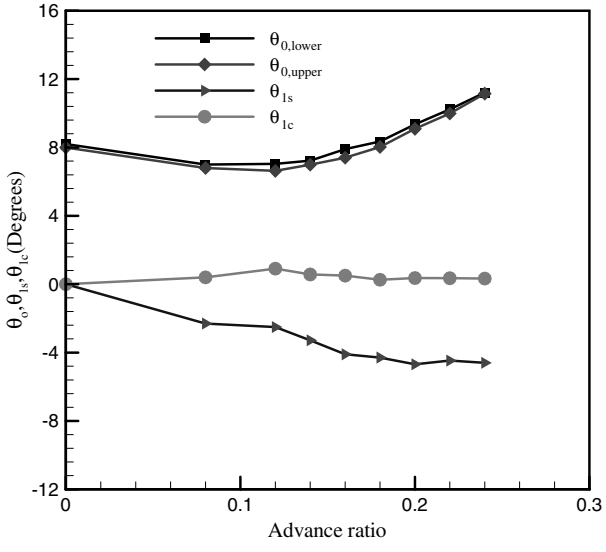


**Fig. 10 Control angles required for trim in forward flight.**

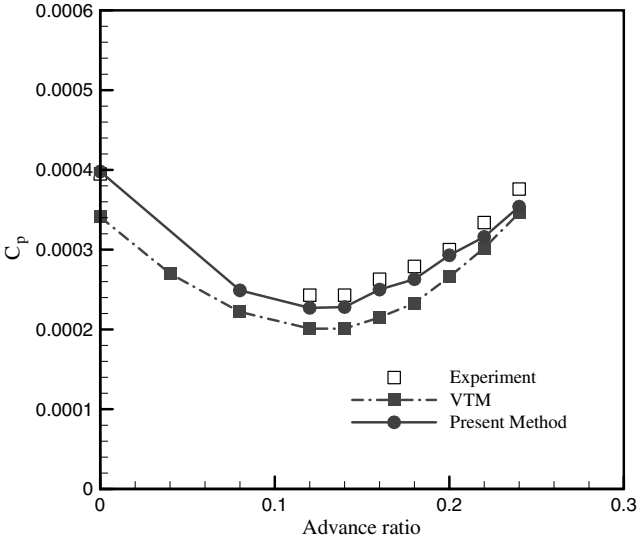


**Fig. 11 Overall power consumption in steady forward flight ($C_T = 0.0048$).**

shown in Fig. 8. It is because that the more accurate vortex trajectories can provide correct induced angle, by which the drag coefficients are read from the table. As shown in the figure, The VTM method seems to yield faster downward movement of the tip vortices compared to the experiments, which may result in the smaller induced velocities on the blades and eventually can lead to the underestimation of the induced angle. On the other hand, the present approach modeled the behavior of the wake very well, which resulted in a better estimation of the profile power.

## IV. Design Parameter Selection and Parametric Studies

The primary mission parameters of a UAV include: endurance, maximum altitude, dimension, weight, and acquisition cost. The preliminary guidelines for the UAV design were concretized from the preliminary study [22]. In this study, the requirement for the overall size of the UAV is that the rotor diameter of the UAV is less than. The maximum takeoff gross weight is set to 10 kg with a minimum payload of 4 kg. The UAV is required to demonstrate hovering capability with a maximum altitude of 500 m and a flight range of 2 km. Maximum duration is expected to be at least 30 min. Table 1 summarizes the requirements for the baseline UAV design. The mission profile of the designed UAV is shown in Fig. 1, focusing on the urban intelligence gathering. The UAV travels 1500 m in 8 min and returns after a 10 min reconnaissance mission (hovering and loitering). The travel time includes forward flight at the cruise speed of 25 km/h and two climbs with a climb rate of 90 mpm. The UAV should be able to stay in the air, hovering, for at least 30 min. Note that these requirements are temporary and can be updated during the development in order to satisfy the users' requirements. To achieve low susceptibility and high maintainability, instead of the engine, the electric motor is selected as the propulsion system. Figure 12 shows a prototype of the coaxial UAV that Pusan National University designed to meet the specified requirements. The analysis in this paper is based on the first version of the rotor configuration, and the current configuration is at the third revision.

**Fig. 12 Configuration of the baseline coaxial rotor UAV.**

It is necessary to perform a sensitivity analysis to investigate the rotor performance in response to the variation of design parameters, such as rotor diameter, rotor spacing, twist, taper ratio, and differential radius. The differential collective pitch angle is not selected as the design parameter. It is because the combination of collective angles of upper and lower rotors is fixed for a given thrust as long as the calculated results are obtained under the condition of zero net yawing moment. The configuration of the baseline rotor blade is determined based on the preliminary study and the statistical database of similar UAVs. The detailed geometric parameters are summarized in Table 2.

### A. Rotor Diameter and Solidity $\sigma$

The autorotation and hovering performance of the rotorcraft can be improved by increasing the rotor diameter. However, it also leads to degradations on the overall dimension, cost, weight and the torque limit of the gear box. The primary objective of this study is to develop a UAV with the smallest rotor diameter that can guarantee a safe landing. Since the UAV under consideration has no surplus battery pack, the coaxial rotor configuration is desired because of its autorotation characteristics. The plots for thrust to power and the figure of merit with respect to the rotor radius ratio are given, as shown in Fig. 13. As expected, the power required for a given thrust decreases as the rotor radius increases. However, the improvement in hovering performance is marginal. This result can be explained by the following equations [3] that Vil'dgrube [23] developed for the coaxial rotors:

$$\frac{C_P}{\sigma} = \frac{1}{4}k_{pr}C_{d_0} + 0.79\left(\frac{C_T}{\sigma}\right)^{3/2}\sigma^{1/2}I_0 \tag{12}$$

$$\mathrm{FM} = \frac{\frac{C_T^{3/2}}{\sqrt{2}}}{C_P} = \frac{(\frac{C_T}{\sigma})^{3/2}\sigma^{1/2}}{\sqrt{2}\cdot C_P/\sigma} \tag{13}$$

where $k_{pr}$ is the taper ratio influence coefficient that accounts for the taper ratio and becomes around 1.0 when the taper ratio is 1.0; $I_0$ is the induced-power correction coefficient, which is affected only by the taper and with the twist remaining the same along the radius. If

**Table 1 Summary of the baseline requirements**

| Requirement | Specifications |
|---|---|
| Dimension | Less than 2 m |
| Maximum duration | 30 min. |
| Maximum hovering ceiling | 500 m |
| Maximum forward speed | 30 km/h |
| Maximum climb speed | 100 m/ min |
| Maximum takeoff gross weight | 10 kg |
| Maximum operational range | 1.5 km |

**Table 2 Configuration of the baseline rotor blade**

| Design parameters | Specifications |
|---|---|
| Root cut | 101 mm |
| Radius $R$ | 786 mm |
| Area $A$ | 1.94 $m^2$ |
| Solidity $\sigma$ | 0.0955 |
| Chord $c$ | 59 mm |
| Airfoil | NACA0015 |

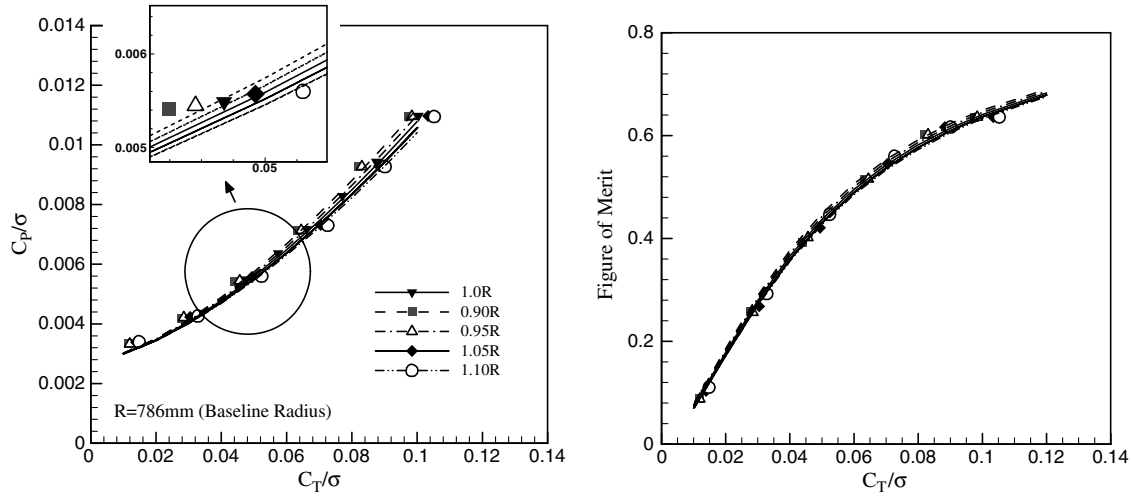


**Fig. 13 Hovering performance vs rotor radius [present method: lines, left: Eq. (12), and right: Eq. (13)].**

$C_T/\sigma$ remains the same, in cases in which the taper, twist, and airfoil are the same, $C_P/\sigma$ is proportional to $\sigma^{1/2}$, as shown in Eq. (12). It is known that the solidity is inversely proportional to the radius, hence, $C_P/\sigma$ becomes inversely proportional to $\sqrt{R}$. As shown in Eq. (13), for the same $C_T/\sigma$, the figure of merit almost does not change. This is because both the numerator and the denominator of Eq. (13) are proportional to $\sigma^{1/2}$. The analysis results exhibit a good agreement with results calculated using Vil'dgrube's [23] formula.

Andrew [24] and Coleman [3] discussed the possibility of improving the coaxial rotor performance through the use of different radii for the upper and lower rotor. It was found from the analytical model that the decrease in the upper rotor radius by 8% could improve the hovering performance, since the fresh air over a larger portion of the lower rotor disc can be provided. Figure 14 shows the comparison of hover performance with respect to differential rotor radii. The lower rotor radii is fixed as baseline, and the upper rotor radii is varied so that radius ratio $R_u/R_l$ has 1.0, 0.9, and 0.8. Figure 14 indicates that the substantial improvement of the rotor performance could occur by differentiating the rotor radii. It is observed that there exists a cross between the cases of $R_u/R_l = 0.8$ and 0.9 at about $C_T = 0.006$, which corresponds to the hovering. All of the data shown in the figure are obtained under torque balance conditions between the two rotors. To guarantee the torque balance, the shorter the upper rotor becomes, the higher pitch angles it should have. Hence, when the total thrust level exceeds some critical value (i.e., $C_T = 0.006$ -, the required power of the upper rotor in $R_u/R_l =$ 0.8 becomes greater than that in $R_u/R_l = 0.9$, due to its higher pitch angle. Though, $R_u/R_l = 0.8$ and $R_u/R_l = 0.9$ has similar performance in the hover region, the rotor system with $R_u/R_l =$ 0.9 shows superior hovering performance over high trust region, which required for axial climb. The numerical results are consistent with the conclusion drawn by Andrew [24] and Coleman [3].

### B. Anhedral Angle Λ

Anhedral angle is usually combined with the sweptback tips. It is known that a 20 deg anhedral can improve the figure of merit (FM) by around 3% by modifying the location the vortex shedding [25]. This improvement is believed to stem from the change in the maximum circulation and the tip vortex position. It is also reported that the anhedral angel can also benefit the rotor performance in forward flight [26]. Figure 15 illustrates the variation of the hovering performance with the anhedral angle, which is implemented at $r/R = 0.9$ of both upper and lower rotors, and set to 10 and 20 deg, respectively. No remarkable improvement of the hovering performance is observed although the rationale is not clear yet. However, the anhedral angle could be considered for noise reduction rather an improving hover performance.

### C. Blade Twist and Taper

The blade twist of the modern helicopter ranges from −8 to −14 deg. The proper use of blade twist can substantially improve the

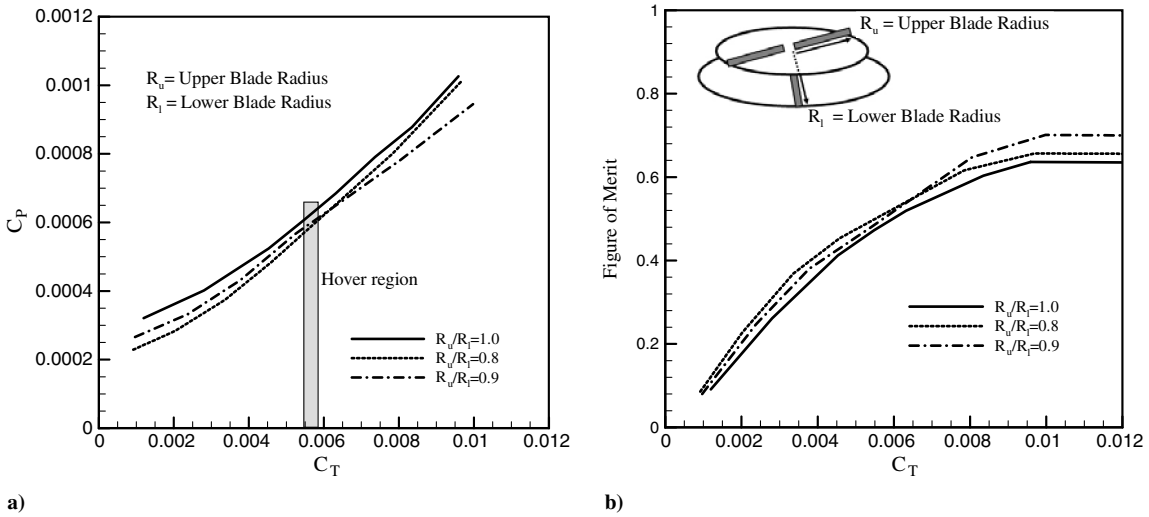


**Fig. 14 Comparison of hovering performance due to differential rotor radii.**

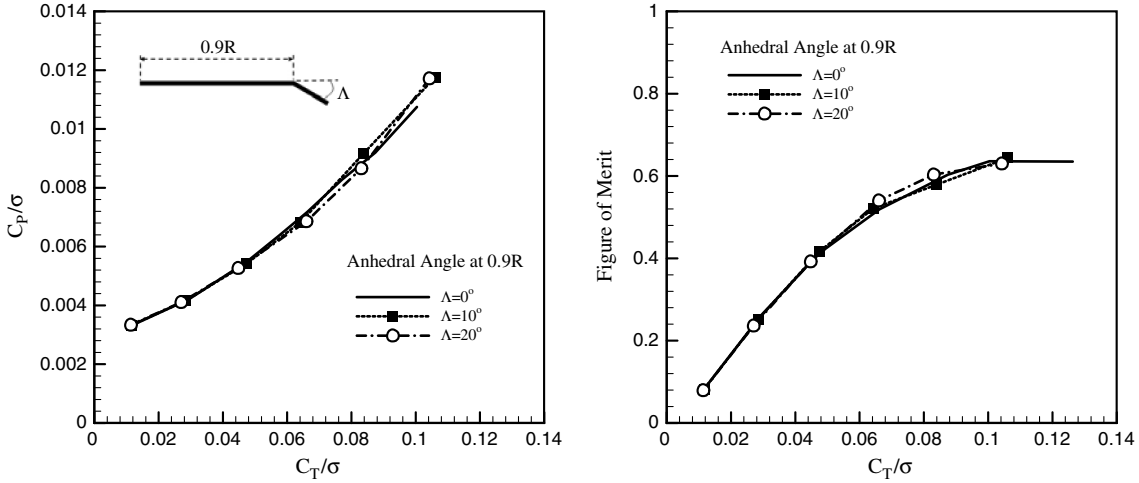


a) b)

**Fig. 15 Hovering performance with anhedral angle.**

figure of merit of the rotor. If the blade twist is too high (greater than 15 deg), the rotor may produce a reduced, or even a negative lift, on the advancing side. It appears that the linear twist range of −10 to −12 deg is good for both the hovering and forward flight [1].

Taper has the same effect as the blade twist in which it is able to minimize the induced drag by making the induced velocity more uniform along the blade span. The combined use of the blade twist and taper could greatly improve the rotorcraft performance. The results for the coaxial rotor with the twists and tapers are shown in Figs. 16 and 17.

As expected, one can see from Figs. 16 and 17 that the figure of merit is generally improved with twist angle and taper increasing. However, when the twist is above $\theta_{tw} = -8$ deg, the significant improvement is not observed on the hover region. Overall, the figure of merit increases by 6.2% as compared to the baseline rotor.

On the other hand, the hovering performance is found to be more sensitive to the taper. This is in agreement with the conclusion drawn by Wachspress and Quackenbush [6]. That is, 5–6% reduction in the induced power is contributed by tapering the outer 50% of blade span. In the present calculation, the performance improvement due to the taper on the whole blade is remarkable with about a 13% increase in figure of merit observed. Even with the increase of taper ratio from 2 to 3, the power reduction is not negligible. It seems that the increased profile power due to low Reynolds number effect at the tip region compensates the reduction of induced power due to taper ratio. With excessive taper ratio, the Reynolds number at the tip region can be significantly decreased, due to the reduced chord length at the tip. The total required power can be significantly increased, due to the increased profile drag due to low Reynolds number at the tip region, which is called *low Reynolds number effect*. To avoid this unfavorable effect, a taper ratio of 2 is chosen in this study, and this is implemented from the root both upper and lower rotors.

### D. Vertical Separation

As discussed by Nagashima and Nakanishi [19] and Wachspress and Quackenbush [6], the vertical separation between the upper and lower rotors appears to have little effect on the hovering performance. In this study, the observation is quantitatively reconfirmed for the coaxial rotor system under consideration. Figure 18 indicates that the hovering performance varies slightly with the increased vertical separation distance when $H/D$ is greater than 0.1. The results seem to support the conclusion drawn by Nagashima and Nakanishi [19] that the variations in separation distance of the coaxial rotors have a slight effect on the hovering performance as long as the vertical separation distance $H/D$ is greater than 0.05. Hence, in this study, the separation distance is kept constant and equals the baseline value, $H/D = 0.120$, which was decided from the original setup of the experimental facility.

### E. Airfoil Selection

Airfoil is one of the most important design parameters in rotor design, since proper choice of airfoil can result in significant

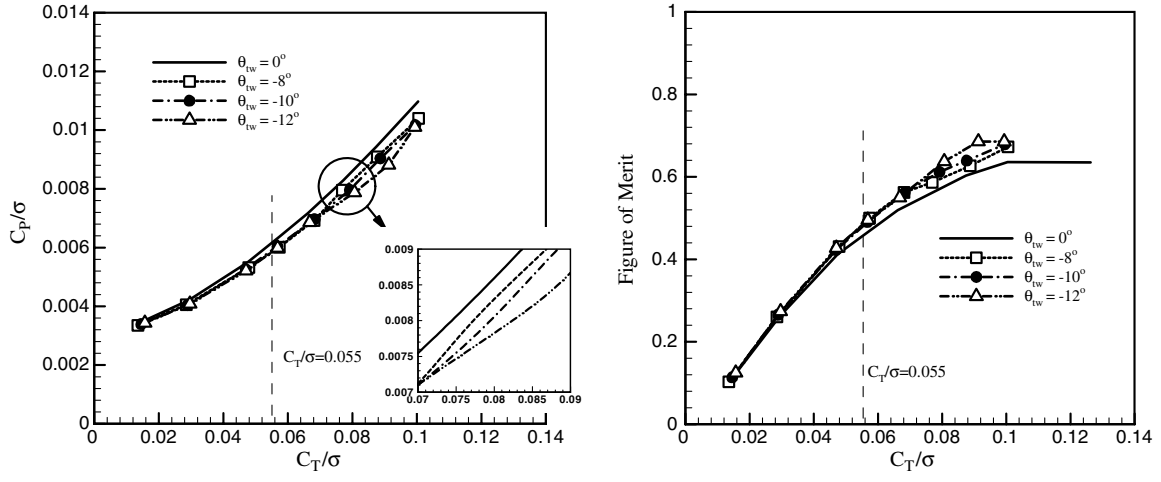


a) b)

**Fig. 16 Hovering performance with twist.**

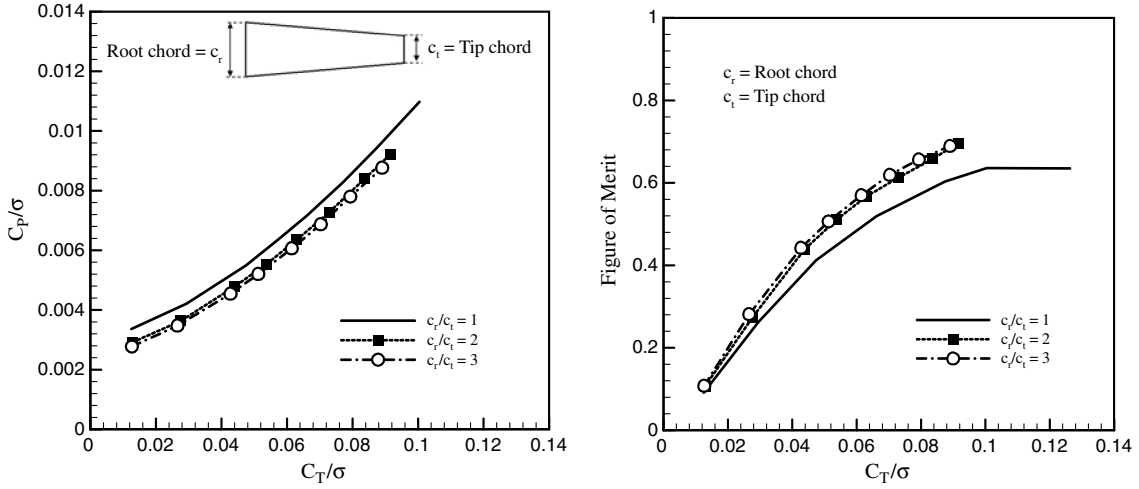


**Fig. 17 Hovering performance with taper.**

performance improvement. Since the operation conditions depend on the design requirements, the performance of the airfoils should be carefully investigated in order to select the appropriate airfoil that best meets the design criteria. To this end, the aerodynamic performance of various airfoils is obtained and evaluated so that the airfoil that can bring the best hovering performance is selected. For numerical computations, the MSES program is exclusively used. This program was developed by Drela and Giles [27] using a coupled viscous/inviscid Euler method and is proven to yield reliable results for airfoil performance at the below-stall angles of attack.

For validation purposes, three different airfoils are selected: ClarkY, SA7036, and ESA, which represent three particular categories of airfoil, respectively. ClarkY is chosen as a representative of the thick airfoil, SA7036 is selected for an opposite representative of the thin airfoil, and ESA airfoil has reversed camber at trailing edge. The calculated results are given in Fig. 19.

It can be seen that the computed results have a good agreement with the experimental data [28], which assures the reliability of further numerical comparisons. The results also show that the MSES program is able to yield reliable results for various airfoils as long as the operating range is below stall.

The required blade loading ($C_T/\sigma$) is determined to satisfy the operational requirements. In this study, that required for hovering is 0.0518, and that required for axial climb is determined by finding the required incremental power. The incremental power required is about 200 W. Hence, the additional power loading is equal to $\Delta C_P/\sigma = 0.0007$. Finally, the required blade loading is determined from the power curve shown in Fig. 14. The blade loading, $C_T/\sigma$ should be 0.060. The advance ratio for the designed vehicle in forward flight is less than 0.1. The power required and the thrust are assumed to be constant in hovering. Hence, the blade loading, $C_T/\sigma$ should lie in the range of $0.0518 \leq C_T/\sigma \leq 0.060$. Representative Reynolds numbers and Mach numbers are $3 \times 10^5$ and 0.24, respectively, which are obtained based on the airfoil at the location where $r/R = 0.75$.

The figure of merit can be simply approximated by using the aerodynamic coefficients of the airfoil. The mean lift coefficient of the rotor is $\bar{C}_L = 6(C_T/\sigma)$ and the drag coefficient is assumed to be constant at a moderate operational condition, i.e., $\bar{C}_D = C_d$. Hence, from the definition, the figure of merit is defined by Eq. (14).

$$\mathrm{FM} = \frac{1}{\kappa + \frac{2.6}{\sqrt{\sigma}}\left(\frac{\bar{C}_L^{3/2}}{\bar{C}_D}\right)^{-1}} \tag{14}$$

It is clear from Eq. (14) that there is a direct relation between FM and the aerodynamic coefficients of the airfoil such as $\bar{C}_L$ and $\bar{C}_D$. Since the required thrust is within the range of $0.0515 \leq C_T/\sigma \leq 0.060$, the mean lift should lie in the range of $0.3 \leq \bar{C}_L \leq 0.36$. Then, the relative performance comparison can be performed in terms of $\bar{C}_L^{3/2}/\bar{C}_D$ and $C_{m_0}$. In the required range of lift coefficient, 18

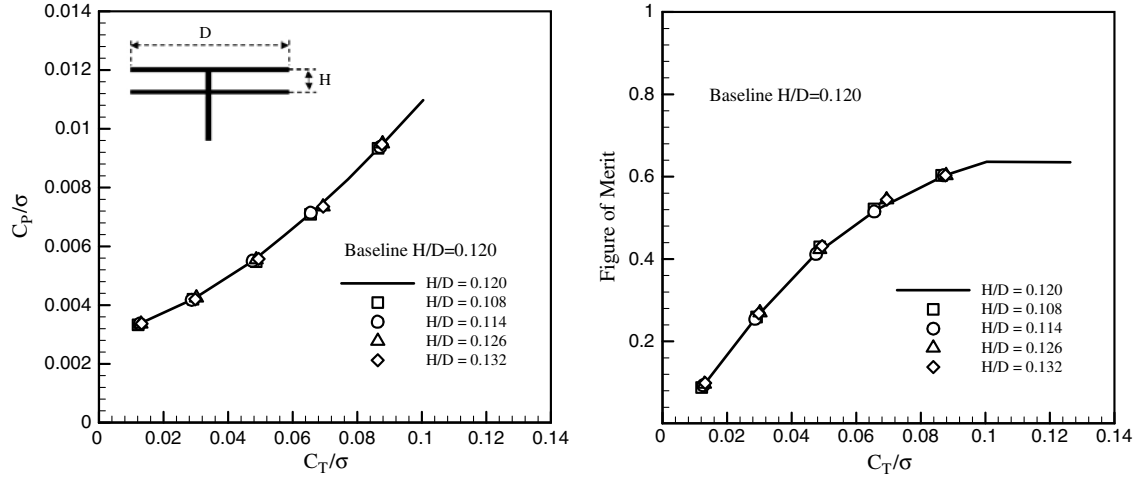


**Fig. 18 Hovering performance with vertical separation.**

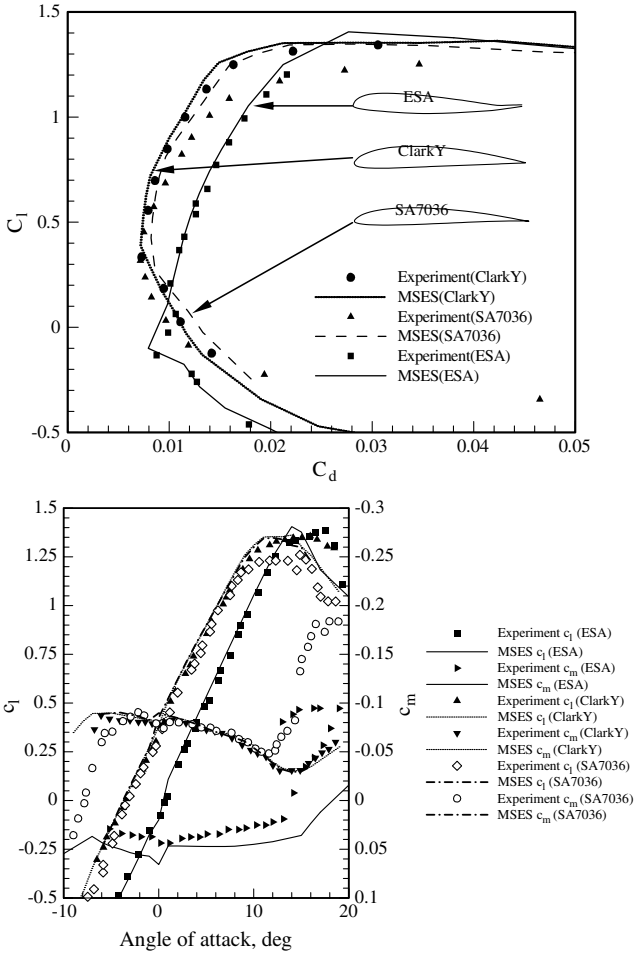


**Fig. 19 Validation of computed results with experiment: ClarkY, SA7036, and ESA.**

airfoils are selected for the relative performance comparison for the hovering condition, and the results are shown in Fig. 20.

In terms of the zero-lift pitching moment and figure of merit, the OA213 and VR 13 airfoils have superior aerodynamic performance under the given flight conditions. The hovering performance variation with the airfoil is given in Fig. 21. It can be seen that the aerodynamic performance is highly affected by the airfoil. That is, with all other conditions kept the same, the change in airfoil can increase the figure of merit up to 11%.

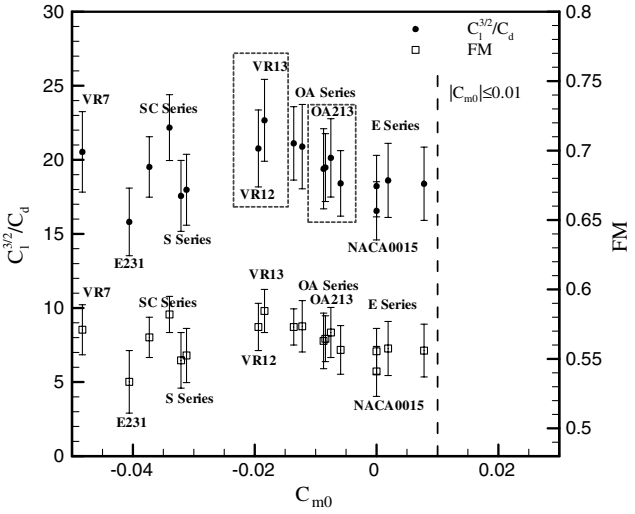


**Fig. 20 Aerodynamic performance of 18 airfoils.**

### F. Statistical Assessment of the Relative Importance of Each Design Parameter

Table 3 lists the design parameters and their ranges for the parametric study. Figure 22 illustrates the relative effect of each design parameter on the rotor performance, represented by the figure of merit and $C_P/\sigma$, for a fixed thrust at 137.34 N. The average rate of change in the performance is calculated between the lower and the upper bounds of each parameter, and its ratio is visualized in the form of a pie graph. The ratio is calculated by using the rate of change in the performance, due to a specific parameter dividing the total effect in the performance, due to all the parameters. The effect of the airfoil is represented as the rate of performance change from NACA0015 to VR13. The results shown in these graphs indicate that the rotor diameter has the greatest effect, on the contrary to the intuition and the physical trend that taper ratio or airfoil may have the largest effect. However, the graphs provide sufficient information to screen out the design parameters whose contribution to the rotor performance is small, when the design analysis is conducted in the design space defined by Table 3.

In Fig. 22, it can be seen that the anhedral angle and $H/D$ have a slight effect on the two performance indices and their effect ratios are 3% and less. Since the anhedral angle is usually combined with sweptback tips, this parameter is insignificant for the rectangular type blade studied in this research. In addition, the vertical separation between the upper and lower rotors is known to have a slight effect on the hovering performance by Nagashima and Nakanishi [19] and Wachspress and Quackenbush [6]. Therefore, the anhedral angle

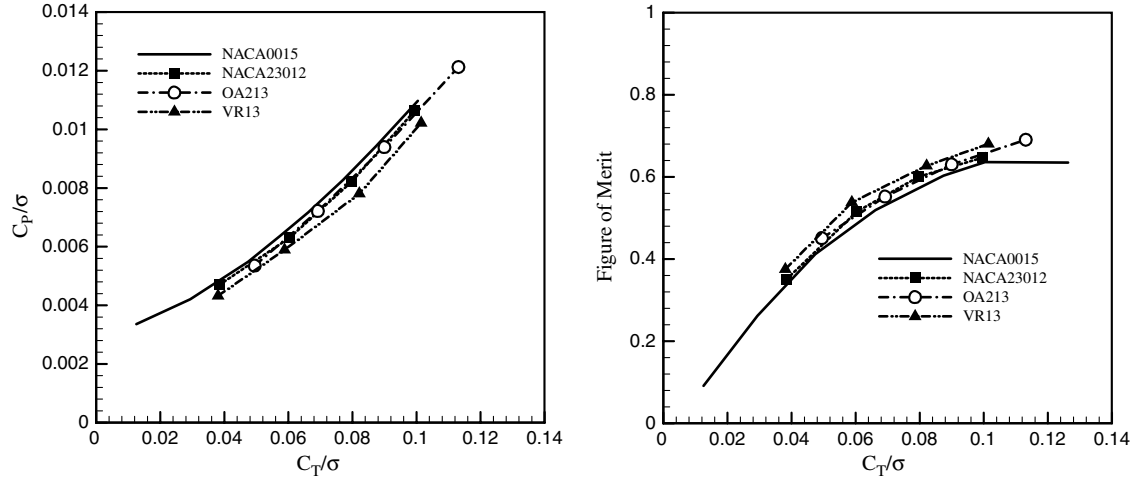


**Fig. 21 Hovering performance with various airfoils.**

**Table 3 Design parameters**

| Design parameters | Lower bound | Upper bound |
|---|---|---|
| Rotor diameter ($D = 1572$ mm) | $0.9D$ | $1.1D$ |
| Differential rotor radii $R_U/R_L$ | 0.8 | 1.0 |
| Anhedral angle, deg | 0 | 20 |
| Twist, deg | −14 | −8 |
| Taper | 1 | 3 |
| Vertical separation $H/D$ | $0.108D$ | $0.132D$ |
| Airfoil | NACA0015, NACA23012, OA213, VR13 | |

and $H/D$ are excluded from the design variables during further studies.

## V. Detailed Formatting Instructions

Figure 23 illustrates the aerodynamic performance of the rotor with a revised platform based on the parametric study on the cases in which the NACA0015 is used as the baseline airfoil and NACA23012 and VR13 are used as new airfoils. The twist is determined to be −10 deg. This is because the rotor with a blade twist between −10 and −12 deg often demonstrates good performance in hovering and forward flight, and there is no significant difference in performance for a rotor with a twist greater than −8 deg. The taper is set at 2 considering the structural safety, although the greater taper is slightly better for the rotor performance. The rotor ratio is determined to be 0.9 as it shows better performance than the rotor with a rotor ratio of 0.8.

As shown in Fig. 23, for the standard airfoil NACA0015, the revised rotor configuration shows about a 15% increase in performance compared to the baseline configuration at the location where $C_T/\sigma$ equals 0.055. Unlike the results shown in Fig. 21, the rotors with revised airfoils of NACA0015 and NACA23012 have little difference in performance. On the other hand, VR13 shows 33% improvement in the figure of merit at the location where $C_T/\sigma$ equals 0.055. The aerodynamic characteristics of the baseline and the revised rotors are listed in Table 4. The table reveals that the power required in terms of $C_P/\sigma$ for revised rotor configuration reduces by 32% under the condition in which thrust equals 137 N. This implies that the low power required during the hovering will lead to increased endurance. However, the autorotation index (AI) of the revised configuration decreases by 7%. The autorotation index, the ratio of the kinetic energy of the main rotor to the overall weight, indicates the autorotation performance of the rotor, and is defined as Eq. (15). In general, AI should be at least 20 for the single-engine helicopters:

$$\mathrm{AI} = \frac{I_R \Omega^2}{2W \cdot \mathrm{DL}} \tag{15}$$

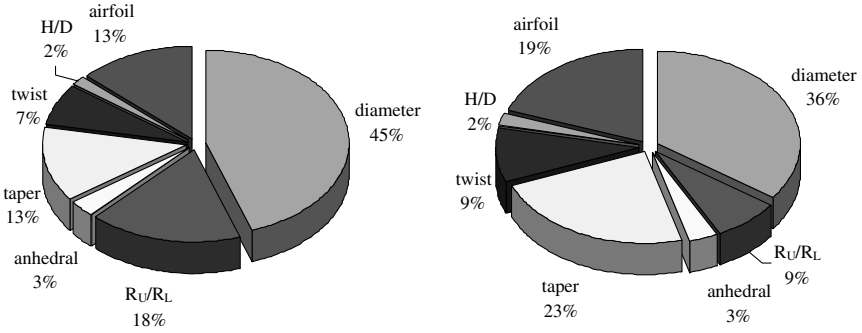


**a) $C_P/\sigma$** **b) Figure of merit**

**Fig. 22 Influence of the design parameters on hovering performance.**

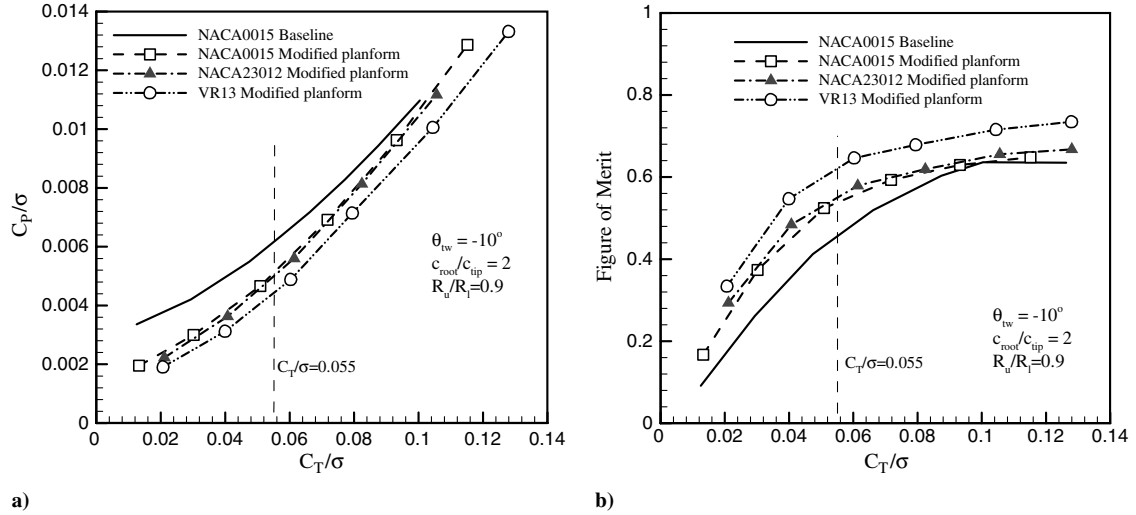


**a)** **b)**

**Fig. 23 Hovering performance for modified configuration with airfoil variation.**

**Table 4 Specifications and performances of two coaxial rotors**

| | Baseline configuration | Modified configuration |
|---|---|---|
| Airfoil | NACA0015 | VR13 |
| Rotor diameter, mm | 1572.00 | 1572.00 |
| $R_u/R_l$ | 1.0 | 0.9 |
| Twist, deg | 0.00 | −10.00 |
| Taper | 1.00 | 2.00 |
| Solidity $\sigma$ | 0.09550 | 0.1008 |
| Figure of merit | 0.4657 | 0.6195 |
| $C_T/\sigma$ | 0.0578 | 0.0548 |
| $C_P/\sigma$ | 0.0065 | 0.0044 |
| Thrust, N | 137.3417 | 137.3433 |
| AI | 9.2863 | 8.6141 |

As the low AI may result in problems in rotorcraft operation, the optimization methods should be employed in the rotor design to develop the optimal configuration with appropriate AI.

In addition, the effect of the revised rotor configuration on the performance in forward flight is also investigated under the condition in which $C_T$ equals 0.0056. Figure 24 shows the control angles for the baseline rotor and the revised rotor obtained from the trim analysis using Newton–Raphson method as Eq. (11). The general trends are similar. In Fig. 25, the change of the rotor power coefficients with the advance ratio is presented. Both rotors have the minimum power coefficient at the point where the advance ratio is 0.12, while the power coefficient of the revised rotor reduces 26%, compared to the baseline rotor. This indicates that the revised rotor not only has better performance when in hovering mode, but also has better performance in forward flight.

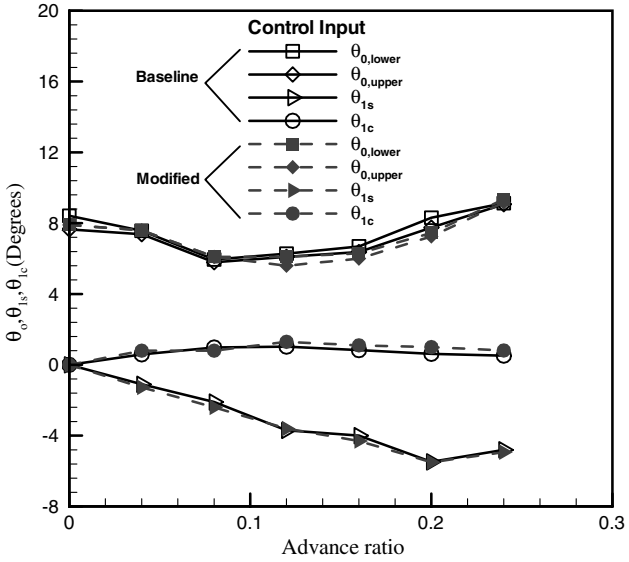


**Fig. 24 Control angles required for trim in forward flight.**

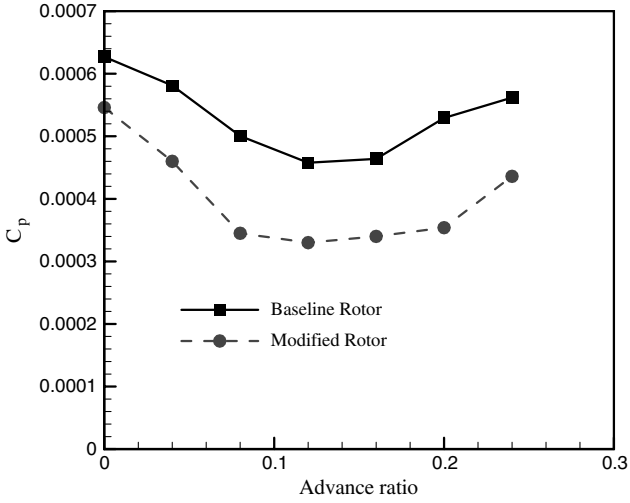


**Fig. 25 Predictions of coaxial rotor power in forward flight.**

## VI. Conclusions

In response to the growing interest in the efficient UAVs, a coaxial rotor system is chosen as a baseline platform for the currently ongoing project. A reliable analytical code based on the source-doublet panel method was developed and validated against the available experimental data. The hovering performance of a coaxial rotor was thoroughly investigated with respect to the various configuration parameters such as taper, twist, differential radii, anhedral, airfoil, and vertical separation. Based on the understanding of the aerodynamic characteristics of the coaxial rotor system, a revised configuration was developed. The relative importance of each design parameter on the performance was investigated as well.

In summary, the following conclusions can be drawn:

1) The numerical code developed for the multirotor analysis is verified as being able to predict the aerodynamic performance of the rotor with good accuracy, which is demonstrated through comparing the calculated result with the experimental data. The drag coefficient correction using the relative Reynolds number and wake instability is found to be essential for the accurate prediction of the power required, especially for a small-scale UAV.

2) In the parametric study, the relation between the coaxial rotor performance indices and design parameters are identified by the sensitivity analysis. The influence of the anhedral angle and $H/D$ on performance indices is less than 3%. On the other hand, the radius, twist, airfoil and taper have significant impact on the performance. The parameter that has the strongest influence on hovering performance is the radius, and the taper parameter has the strongest influence if the radius is fixed.

3) The baseline rotor configuration is modified and its hovering performance is analyzed. About 33% hovering performance improvement with VR13 airfoil is obtained at the design point where $C_T/\sigma$ equals 0.055, which implies that further research is needed to be done for performance improvement using the design optimization method.

## Acknowledgments

This study has been supported by the Korea Aerospace Research Institute (KARI) under Korean Helicopter Program (KHP) Dual-Use Component Development Program funded by the Ministry of Knowledge.

## References

[1] Leishman, J. G., *Principles of Helicopter Aerodynamics*, 2nd ed., Cambridge Univ. Press, Cambridge, England, U.K., 2006.

[2] Preator, R., Leishman, J. G., and Baldwin, G. D., "Conceptual Design Studies of a Mono Tiltrotor (MTR) Architecture," *Proceedings of the 60th Annual National Forum of the American Helicopter Society* [CD-ROM], AHS International, Alexandria, VA, 2004.

[3] Coleman, C. P., "A Survey of Theoretical and Experimental Coaxial Rotor Aerodynamic Research," NASA TP 3675, 1997.

[4] Kim, H. W., and Brown, R. E., "Coaxial Rotor Performance and Wake Dynamics in Steady and Maneuvering Flight," *American Helicopter Society 62nd Annual Forum* [CD-ROM], AHS International, Alexandria, VA, 2006.

[5] Leishman, J. G., and Ananthan, S., "Aerodynamic Optimization of a Coaxial Prop Rotor," *American Helicopter Society 62nd Annual Forum* [CD-ROM], AHS International, Alexandria, VA, 2006.

[6] Wachspress, D. A., and Quackenbush, T. R., "Impact of Rotor Design on Coaxial Rotor Performance, Wake Geometry and Noise," *American Helicopter Society 62nd Annual Forum* [CD-ROM], AHS International, Alexandria, VA, 2006.

[7] Anderson, J. D., *Modern Compressible Flow with Historical Perspective*, 3rd ed., McGraw–Hill, New York, 2003, pp. 324–335.

[8] Katz, J., and Plotkin, A., *Low-Speed Aerodynamics*, 2nd ed., Cambridge Univ. Press, Cambridge, England, U.K., 2001.
[9] Hess, J. L., "Calculation of Potential Flow About Arbitrary Three-Dimensional Lifting Bodies," McDonnell Douglas TR MDC J5679-02, Long Beach, CA, 1972.
[10] Leishman, J. G., Baker, A., and Coyne, A., "Measurements of Rotor Tip Vortices Using Three-Component Laser Doppler Velocimetry," *Journal of the American Helicopter Society*, Vol. 41, No. 4, 1996, pp. 342–353. doi:10.4050/JAHS.41.342
[11] Vatistas, G. H., Kozel, V., and Mih, W., "A Simpler Model for Concentrated Vortices," *Experiments in Fluids*, Vol. 11, 1991, pp. 73–76. doi:10.1007/BF00198434
[12] Lee, S. K., "Aerodynamic Analysis of Rotor Blades and Ducted Fan Using Improved Panel and Time-Marching Free Wake Coupling Method," M.S. Thesis, Dept. of Mechanical Engineering, Div. of Aerospace Engineering, Korea Advanced Institute of Science and Technology, Daejeon, ROK, 2003.
[13] Rosen, A., and Graber, A., "Free Wake Model of Hovering Rotors Having Straight or Curved Blades," *Journal of the American Helicopter Society*, Vol. 33, No. 3, 1988, pp. 11–19. doi:10.4050/JAHS.33.11
[14] Summa, J. M., and Maskew, B., "New Method for the Calculation of Hover Air Loads," *Fifth European Rotorcraft and Powered Lift Aircraft Forum*, Amsterdam, 1979.
[15] Bagai, A., and Leishman, J. G., "Rotor Free-Wake Modeling Using a Relaxation Technique-Including Comparisons with Experimental Data," *American Helicopter Society 50th Annual Forum*, AHS International, Alexandria, VA, 1994.
[16] Quaranta, G., Bindolino, G., Masarati, P., and Mantegazza, P., "Toward a Computational Framework for Rotorcraft Multi-Physics Analysis: Adding Computational Aerodynamics to Multibody Rotor Models," *30th European Rotorcraft Forum* [CD-ROM], Marseilles, France, 2004.
[17] Caradonna, F. X., and Tung, C., "Experimental and Analytical Studies of a Model Helicopter Rotor on Hover," NASA TM 81232, 1981.
[18] Harrington, R. D., "Full Scale Tunnel Investigation of the Static Thrust Performance of a Coaxial Helicopter Rotor," NACA TN 2318, 1951.
[19] Nagashima, T., and Nakanishi, K., "Optimum Performance and Wake Geometry of Coaxial Rotor in Hover," *7th European Rotorcraft and Powered Lift Forum*, 1991.
[20] Landgrebe, A. J., "An Analytical and Experimental Investigation of Helicopter Rotor Hover Performance and Wake Geometry Characteristics," U.S. Army Air Mobility Research and Development Lab., TR 71-24, Eustis Directorate, Fort Eutis, VA, 1971.
[21] Dingeldein, R. C., "Wind-Tunnel Studies of the Performance of Multirotor Configurations," NACA TN 3236, 1954.
[22] Byun, Y., Song, J., Lee, B., Kim, S., Song, W., and Kang, B., "Design and Integration of Small Coaxial Unmanned Aerial Vehicle," *AUVSI North America 2007*, Washington, D.C., Aug. 2007.
[23] Vil'dgrube, L. S., *Vertolety, Raschet Integral'nykh Aerodynamicheskikh Kharakteristick i Letnomekhanicheskikh Danykh*, Mashinostroyeniye, Moscow, 1977 (in Russian).
[24] Andrew, M. J., "Coaxial Rotor Aerodynamics in Hover," *Vertica*, Vol. 5, No. 2, 1981, pp. 163–172.
[25] Vuillet, A., "Rotor and Blade Aerodynamic Design," AGARD Rept. R-781, Neuilly-sur-Seine, France, 1990.
[26] Desopper, A., Lafon, P., Philippe, J. J., and Prieur, J., "Effect of an Anhedral Sweptback Tip on the Performance of a Helicopter Rotor," *Vertica*, Vol. 12, No. 4, 1988, pp. 345–355.
[27] Drela, M., and Giles, M. B., "ISES: A Two Dimensional Viscous Aerodynamic Design and Analysis Code," AIAA Paper 87-0424, 1987.
[28] Lyon, C. A., Broeren, A. P., Giguere, P., Gopalarathnam, A., and Selig, M. S., *Summary of Low-Speed Airfoil Data*, Vol. 3, SoarTech, Virginia Beach, VA, 1997.